

## Pulsar emission amplified and resolved by plasma lensing in an eclipsing binary

Robert Main<sup>1,2,3</sup>, I-Sheng Yang<sup>3,4</sup>, Victor Chan<sup>1</sup>, Dongzi Li<sup>3,5</sup>, Fang Xi Lin<sup>3,5</sup>, Nikhil Mahajan<sup>1</sup>, Ue-Li Pen<sup>3,6,2,4</sup>, Keith Vanderlinde<sup>1,2</sup> & Marten H. van Kerkwijk<sup>1</sup>

**Radio pulsars scintillate because their emission travels through the ionized interstellar medium via multiple paths, which interfere with each other. It has long been realized that the scattering screens responsible for the scintillation could be used as “interstellar lenses” to localize pulsar emission regions<sup>1,2</sup>. Most scattering screens, however, only marginally resolve emission components, limiting results to statistical inferences and detections of small positional shifts<sup>3–5</sup>. Since screens situated close to the source have better resolution, it should be easier to resolve emission regions of pulsars located in high density environments such as supernova remnants<sup>6</sup> or binaries in which the pulsar’s companion has an ionized outflow. Here, we report events of extreme plasma lensing in the “Black Widow” pulsar, PSR B1957+20, near the phase in its 9.2 hour orbit in which its emission is eclipsed by its companion’s outflow<sup>7–9</sup>. During the lensing events, the flux is enhanced by factors of up to 70–80 at specific frequencies. The strongest events clearly resolve the emission regions: they affect the narrow main pulse and parts of the wider interpulse differently. We show that the events arise naturally from density fluctuations in the outer regions of the outflow, and infer a resolution of our lenses comparable to the pulsar’s radius, about 10 km. Furthermore, the distinct frequency structures imparted by the lensing are reminiscent of what is observed for the repeating fast radio burst FRB 121102, providing observational support for the idea that this source is observed through, and thus at times strongly magnified by, plasma lenses<sup>10</sup>.**

On 2014 June 13–16, we took 9.5 hours of data of PSR B1957+20 with the 305-m William E. Gordon Telescope at the Arecibo observatory, at observing frequency of 311.25–359.25 MHz (see Methods). These data were previously searched for giant pulses<sup>11</sup> – sporadically occurring, extremely bright pulses, which are much shorter than regular pulses ( $\lesssim 1 \mu\text{s}$  compared to 10s of  $\mu\text{s}$ ). While we found many giant pulses at all orbital phases, we noticed that the incidence rate of bright pulses was much higher leading up to and following the radio eclipse.

As can be seen in Figure 1, most of the pulses near eclipse do

not look like giant pulses but rather like brighter regular pulses – they are bright over a large fraction of the pulse profile, and most tellingly, occur in groups spanning several 1.6 ms pulse rotations, suggesting the underlying events last of order 10 ms. Their properties seem similar to the hitherto mysterious bright pulses associated with the eclipse of PSR J1748–2446A<sup>12</sup>, suggesting a shared physical mechanism.

High-magnification events are often chromatic, as can be seen from the colors in Figure 1 (which reflect 16 MHz sub-bands), and is borne out more clearly by the spectra shown in Figure 2: some show frequency widths comparable to our 48 MHz band, peaking at low or high frequency, while others show strong frequency evolution, in some cases tracing out a slope in frequency-time space, in others a double-peaked profile.

For many high-magnification events, the magnification is not uniform across the pulse profile. The bottom panel of Figure 1 shows this dramatically: at 0.2 s, the main pulse is greatly magnified over 5 pulses, while the entire interpulse is barely affected. In addition, the components of the broad interpulse are often magnified differently from each other, as can be seen most readily in the magnified events in Figure 3. Thus, the events resolve the pulsar’s various emission regions.

The most strongly magnified events occur within three specific time spans, each lasting for  $\sim 5$  minutes, around orbital phase  $\phi = 0.20$ ,  $\phi = 0.30$ , and  $\phi = 0.32$  (see Figure 1); here,  $\phi = 0.25$  corresponds to superior conjunction of the pulsar in its 9.2-hour orbit<sup>7</sup> and the duration of the eclipses at 350 MHz is about 40 to 60 minutes<sup>7–9</sup>, or  $\Delta\phi \simeq 0.1$  (a sketch of the system geometry is shown in Extended Data Figure 1). In each time span, we observe only small overall frequency-dependent time delays, of order  $10 \mu\text{s}$ , which indicate modest increases in electron column density, with dispersion measures (DM) of  $\sim 10^{-4} \text{ pc/cm}^3$  (see Figure 1 as well as Extended Data Figure 3). Intriguingly, at times when the delays are longer and the DM thus higher – right before and after eclipse, and in between the two post-eclipse periods of strong lensing, at  $\phi \simeq 0.31$  – the magnifications are less dramatic, only up to a factor of a few, and correlated over much longer timescales, of order 100 ms. After the main lensing periods, up to  $\phi \simeq 0.36$ , flux variations remain correlated, suggesting even weaker events are still present (examples of lensing in the aforementioned regions are shown in Extended Data Figure 4).

To determine whether the magnification events could be due to lensing by inhomogeneities in the companion’s outflow, we first measured the excess delay due to dispersion at a time resolution of 2 s, the shortest at which we can measure it reliably (see Methods). We find that during the periods of strong magnification events, the delay fluctuates by  $\sim 1 \mu\text{s}$  on this timescale. Assuming the relative velocity between the pulsar and the companion’s outflow is roughly the orbital velocity, 360 km/s (ref.<sup>13</sup>), the 2 s timescale corresponds to a spatial scale  $\Delta x \simeq 720 \text{ km}$ . For

<sup>1</sup>Department of Astronomy and Astrophysics, University of Toronto, 50 St. George Street, Toronto, ON M5S 3H4, Canada

<sup>2</sup>Dunlap Institute for Astronomy and Astrophysics, University of Toronto, 50 St. George Street, Toronto, ON M5S 3H4, Canada

<sup>3</sup>Canadian Institute for Theoretical Astrophysics, University of Toronto, 60 St. George Street, Toronto, ON M5S 3H8, Canada

<sup>4</sup>Perimeter Institute for Theoretical Physics, 31 Caroline Street North, Waterloo, ON N2L 2Y5, Canada

<sup>5</sup>Department of Physics, University of Toronto, 60 St. George Street, Toronto, ON M5S 1A7, Canada

<sup>6</sup>Canadian Institute for Advanced Research, 180 Dundas St West, Toronto, ON M5G 1Z8, Canada

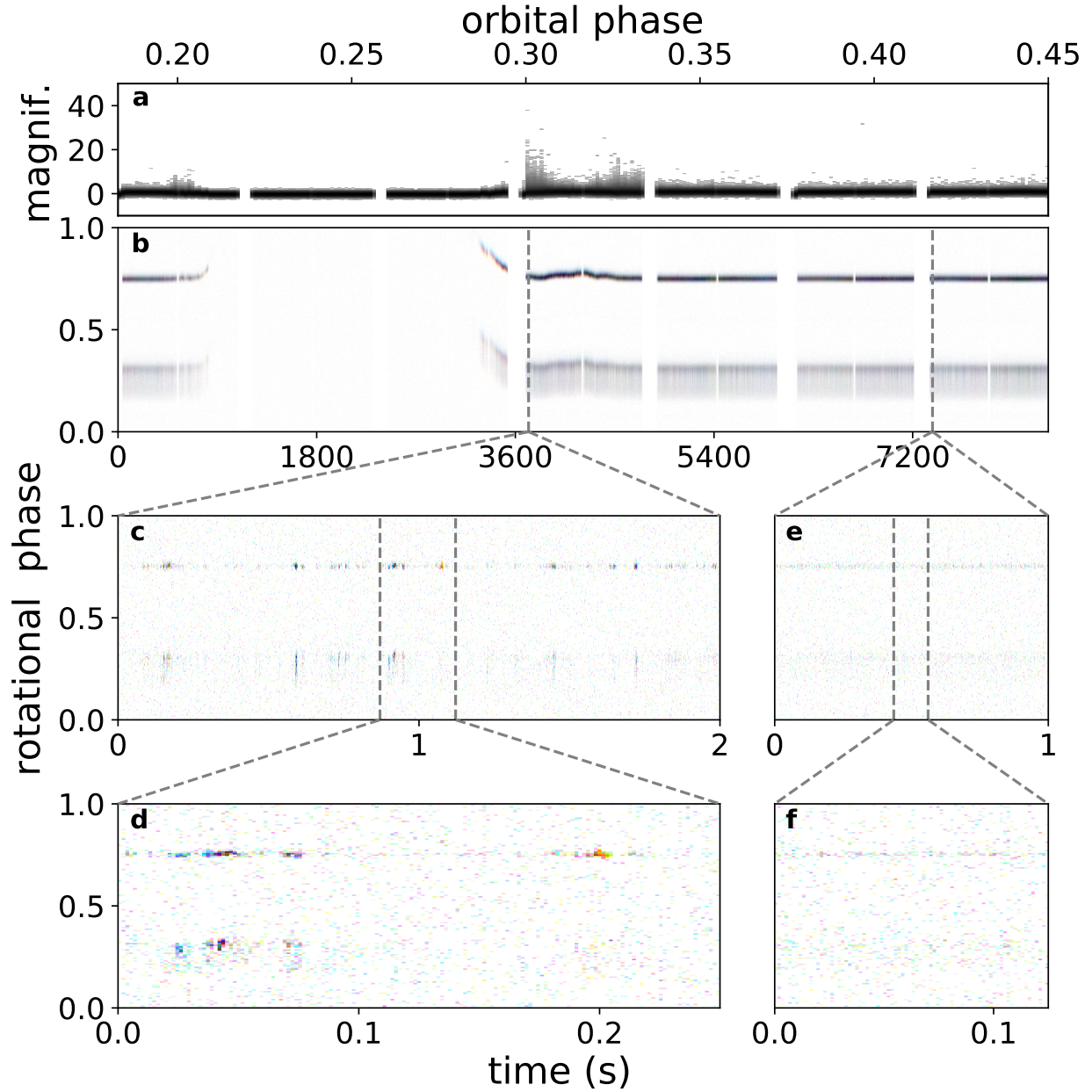


Figure 1: **Strong lensing of the pulsar.** **a**, Magnification distributions for the main pulse, in 10s time bins, showing periods of lensing near ingress and egress of the eclipse of the pulsar by its companion's outflow. The colorbar is logarithmic, to help individual bright pulses stand out. **b**, Pulse profiles as a function of time, averaged over 10 s and in 128 phase bins. Cyan, yellow, and magenta represent contiguous 16 MHz sub-bands, from low to high frequency. Near eclipse, plasma dispersion causes frequency-dependent delays. Gaps in the data correspond to calibrator scans. **c**, **d**, Enlargements in which each time bin corresponds to an individual, 1.6ms pulse. One sees extreme, chromatic lensing in which pulses are magnified by an order of magnitude over tens of ms; the brightest event is magnified by a factor of  $\sim 40$  across our highest frequency sub-band. In some events, the main pulse and interpulse are clearly affected differently, indicating that different emission regions corresponding to these are resolved by the lensing structures. **e**, **f**, Enlargements for a quiescent period for comparison.

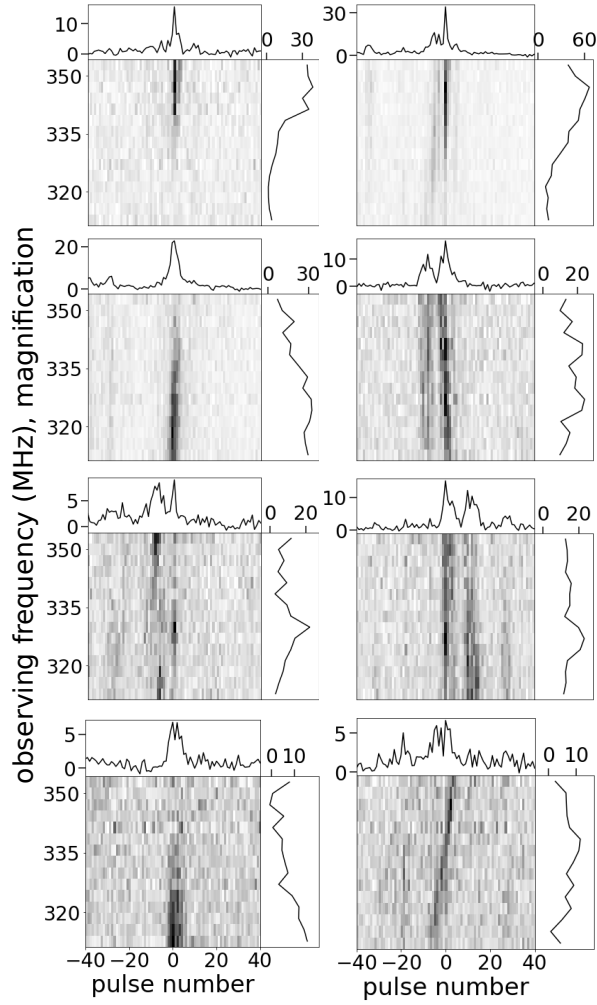


Figure 2: **A range of spectral behavior in lensing events.** Power spectra, binned to 3 MHz, of the main pulse in consecutive 1.6 ms rotations, for selected lensing events from eclipse egress. The top panels show the average magnification in each main pulse, and the side panels the magnification spectra of the brightest pulse (i.e., that of pulse number 0).

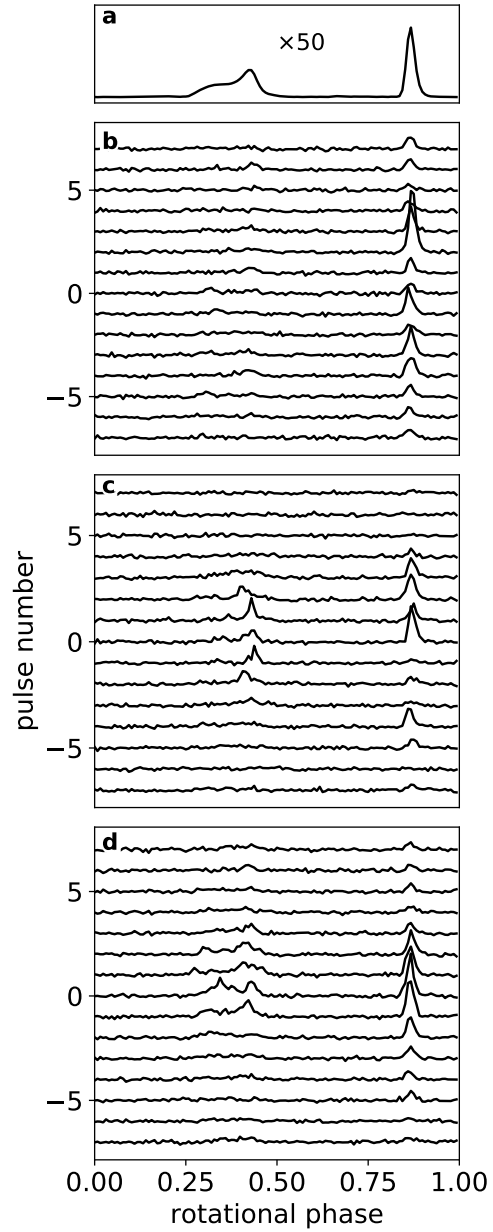


Figure 3: **Profiles of lensing events.** **b, c, d,** Frequency-averaged pulse profiles surrounding bright events (using 128 phase bins). One sees that the events resolve the magnetosphere: the main pulse and interpulse are affected differently, as are parts within the interpulse. **a,** Average pulse profile of a 9 minute quiescent region, scaled up by a factor of 50 for comparison purposes.

this scale, the expected geometric delay is  $\Delta x^2/2ac \simeq 0.5 \mu\text{s}$  (where  $a = 6.4\text{lt-sec}$  is the orbital separation and  $c$  the speed of light). Since this is comparable to the observed dispersive delays, lensing is expected.

To model the magnified pulses, we treat the signal using a standard wave optics formalism. The electric field received by an observer is the sum of the electric field of the source across the lens plane, with the phase at every point determined by both geometric and dispersive delays. When a large area on the plane has (nearly) stationary phase, the electric field combines coherently leading to a strongly magnified image, with the magnification  $\mu$  proportional to the area squared. Since dispersive and geometric delays scale differently with frequency  $\nu$ , a plasma lens cannot be in focus over all frequency, but will impart a characteristic frequency width. This width will be smaller for larger magnification, with the precise scaling depending on the extent to which the lens is elliptic:  $\Delta\nu/\nu \sim 1/\mu$  for a very elongated, effectively linear lens, and  $\Delta\nu/\nu \sim 1/\sqrt{\mu}$  for a (roughly) circular one. In strong lensing, one generically expects multiple images to contribute, and thus caustics to form, which can lead to a slope in time-frequency space, double-peaked spectra, as well as other interference effects (see Methods). All of these are consistent with the behavior seen in the measured spectra of the magnified pulses in Figure 2.

For any lens, different pulse components will be magnified differently if they arise from regions which have projected separations larger than the lens’s resolution. We can make a quantitative estimate of the lens resolution using the magnifications of the events. Continuing to assume the lens is roughly co-located with the companion, i.e., at the orbital separation  $a$ , the resolution of the lens for given magnification would be  $\sim 1.9R_1/\mu^{1/2}$  for a linear lens, or  $\sim 1.9R_1/\mu^{1/4}$  for a circular one, where  $R_1 \equiv \sqrt{\lambda a/\pi}$ , or 23 km at our observing wavelength  $\lambda = c/\nu \simeq 90\text{ cm}$  (see Methods for a derivation). A peak magnification of, eg.,  $\mu = 50$ , then corresponds to a physical resolution of  $\sim 6\text{ km}$  for a linear lens, or  $\sim 17\text{ km}$  for a circular one.

The inferred resolution is comparable to the  $\sim 10\text{ km}$  radius of the neutron star, and substantially smaller than the light-cylinder radius,  $R_{LC} \equiv cP/2\pi = 76\text{ km}$ , where the velocity of co-rotating magnetic fields approaches the speed of light, bounding the magnetosphere in which pulsar emission is thought to originate<sup>14</sup>. Thus, the lensing offers the opportunity to map the emission geometry.

Qualitatively, since the main pulse and interpulse, as well as parts of the wide interpulse beam, are sometimes magnified very differently, the inferred resolution is a lower limit to both the projected separation between the main pulse and the interpulse, and to the size of the interpulse. Perhaps not unexpectedly, the spatial separations do not seem to map directly to rotational phase: we see similar differences between the main pulse and the interpulse, which are separated by half a rotation, and between parts of the interpulse, which are separated by only  $\sim 0.1$  rotation. This may indicate that the interpulse consists of multiple components, which are not located close together in space.

Combining the lens resolution with the timescale of the lensing events allows us to constrain the projected relative velocity

between the lens and the pulsar. A priori, one might expect the outflow velocity to be slow, in which case the relative velocity would just be the orbital motion of  $\sim 360\text{ km s}^{-1}$ . Given that strong magnification events typically last about 10 ms, this would then imply a resolution of  $\sim 4\text{ km}$ , not dissimilar from what we find above, thus suggesting that the assumption of a slow outflow velocity is reasonable. By combining different constraints between the duration and frequency widths of lensing events, we can set a quantitative limit to the relative velocity (see Methods for a derivation), of

$$v > 0.5 \frac{R_1}{\Delta t_{\text{HWHM}}} \left( \frac{\Delta\nu}{\nu} \right)_{\text{HWHM}}^{1/2} \gtrsim 360\text{ km/s}, \quad (1)$$

where for the numerical value we use that the tightest constraints come from the shortest, least chromatic events, which have frequency widths  $(\Delta\nu/\nu)_{\text{HWHM}} \simeq 0.1$ , and durations  $\Delta t_{\text{HWHM}} \simeq 10\text{ ms}$  (measured as Half Width at Half Maximum [HWHM]; see Figure 2). This approximate limit equals the relative orbital velocity, which implies that the outflow velocity can be (but does not have to be) small in the rest frame of the companion.

Our results offer many avenues of further research. Ideally, one would use the lensing to map the pulsar magnetosphere. This requires better constraints on the lenses, e.g., from observations over several eclipses at a range of frequencies. Further observations may also shed light on the eclipse mechanism. E.g., if it is cyclo-synchrotron absorption, large magnetic fields, of  $\sim 20\text{ G}$ , are required<sup>15</sup>, which would impart measurable polarization dependence of the lensing events. Furthermore, combining density and velocity into a mass-loss rate of the outflow, one can infer the life-time, and thus the final fate, of these systems.

Finally, our observations establish that radio pulses can be strongly amplified by lensing in local ionized material. This adds support for the proposal that fast radio bursts (FRBs) can be lensed by host galaxy plasma, leading to variable magnification, narrow frequency structures, and clustered arrival times of highly amplified (and thus observable) events<sup>10</sup>. Evidence for high-density environments includes that FRB 110523 is scattered within its host galaxy<sup>16</sup>, and that FRB 121102 has been localized to a star-forming region<sup>17,18</sup>, in an extreme and dynamic magneto-ionic environment<sup>19</sup>. Indeed, the latter’s repeating bursts have spectra<sup>20–22</sup> remarkably similar to those shown in Figure 2 (e.g., compare with Figure 2 of ref. <sup>20</sup>), and, like those bursts, the brightest pulses in PSR B1957+20 are highly clustered in time.

1. Lovelace, R. V. E. *Theory and analysis of interplanetary scintillations*. Ph.D. thesis, Thesis Fac. Graduate School Cornell Univ. Ithaca N.Y. 405 p. (1970).
2. Backer, D. C. Interstellar scattering of pulsar radiation. I - Scintillation. *Astronomy & Astrophysics* **43**, 395–404 (1975).
3. Gwinn, C. R. *et al.* Size of the Vela Pulsar’s Emission Region at 18 cm Wavelength. *Astrophysical Journal* **758**, 7 (2012). 1208.0040.

4. Johnson, M. D., Gwinn, C. R. & Demorest, P. Constraining the Vela Pulsar's Radio Emission Region Using Nyquist-limited Scintillation Statistics. *Astrophysical Journal* **758**, 8 (2012). 1208.5485.
  5. Pen, U.-L., Macquart, J.-P., Deller, A. T. & Brisken, W. 50 picoarcsec astrometry of pulsar emission. *Monthly Notices of Royal Astronomical Society* **440**, L36–L40 (2014). 1301.7505.
  6. Main, R. *et al.* Mapping the Emission Location of the Crab Pulsar's Giant Pulses. *ArXiv e-prints* (2017). 1709.09179.
  7. Fruchter, A. S., Stinebring, D. R. & Taylor, J. H. A millisecond pulsar in an eclipsing binary. *Nature* **333**, 237–239 (1988).
  8. Fruchter, A. S. *et al.* The eclipsing millisecond pulsar PSR 1957 + 20. *Astrophysical Journal* **351**, 642–650 (1990).
  9. Ryba, M. F. & Taylor, J. H. High-precision timing of millisecond pulsars. II - Astrometry, orbital evolution, and eclipses of PSR 1957 + 20. *Astrophysical Journal* **380**, 557–563 (1991).
  10. Cordes, J. M. *et al.* Lensing of Fast Radio Bursts by Plasma Structures in Host Galaxies. *Astrophysical Journal* **842**, 35 (2017). 1703.06580.
  11. Main, R., van Kerkwijk, M., Pen, U.-L., Mahajan, N. & Vanderlinde, K. Descattering of Giant Pulses in PSR B1957+20. *Astrophysical Journal Letters* **840**, L15 (2017). 1703.05176.
  12. Bilous, A. V., Ransom, S. M. & Nice, D. J. Pulsar in Ter5 A binary system: timing and single-pulse study. In Burgay, M., D'Amico, N., Esposito, P., Pellizzoni, A. & Possenti, A. (eds.) *American Institute of Physics Conference Series*, vol. 1357 of *American Institute of Physics Conference Series*, 140–141 (2011).
  13. van Kerkwijk, M. H., Breton, R. P. & Kulkarni, S. R. Evidence for a Massive Neutron Star from a Radial-velocity Study of the Companion to the Black-widow Pulsar PSR B1957+20. *Astrophysical Journal* **728**, 95 (2011). 1009.5427.
  14. Ginzburg, V. L. & Zhelezniakov, V. V. On the pulsar emission mechanisms. *Annual Review of Astron and Astrophys* **13**, 511–535 (1975).
  15. Thompson, C., Blandford, R. D., Evans, C. R. & Phinney, E. S. Physical processes in eclipsing pulsars: Eclipse mechanisms and diagnostics. *Astrophysical Journal* **422**, 304–335 (1994).
  16. Masui, K. *et al.* Dense magnetized plasma associated with a fast radio burst. *Nature* **528**, 523–525 (2015). 1512.00529.
  17. Tendulkar, S. P. *et al.* The Host Galaxy and Redshift of the Repeating Fast Radio Burst FRB 121102. *Astrophysical Journal Letters* **834**, L7 (2017). 1701.01100.
  18. Bassa, C. G. *et al.* FRB 121102 Is Coincident with a Star-forming Region in Its Host Galaxy. *Astrophysical Journal Letters* **843**, L8 (2017). 1705.07698.
  19. Michilli, D. *et al.* An extreme magneto-ionic environment associated with the fast radio burst source FRB 121102. *Nature* **553**, 182–185 (2018). 1801.03965.
  20. Spitler, L. G. *et al.* A repeating fast radio burst. *Nature* **531**, 202–205 (2016). 1603.00581.
  21. Scholz, P. *et al.* The Repeating Fast Radio Burst FRB 121102: Multi-wavelength Observations and Additional Bursts. *Astrophysical Journal* **833**, 177 (2016). 1603.08880.
  22. Law, C. J. *et al.* A Multi-telescope Campaign on FRB 121102: Implications for the FRB Population. *Astrophysical Journal* **850**, 76 (2017). 1705.07553.
- Author Contributions** R. M. discovered the magnified pulses; wrote the majority of the manuscript; and created the figures. I-S. Y. developed and wrote the sections on wave optics formalism in Methods; M. H. v. K and U-L. P. guided the analysis and interpretation of the results; M. H. v. K. also helped write the manuscript and influenced the content and presentation of the figures; F-X. L., V. C., and K. V. quantified the excess DM associated with the eclipse. N. M. wrote the code used to produce the coherently de-dispersed single pulse profiles used in this analysis, and derived an improved orbital ephemeris relative to which time delays are measured. D. L. worked on criteria to systematically separate giant pulses from pulses magnified by plasma lensing. All authors contributed to the interpretation of results.
- Competing Interests** The authors declare that they have no competing financial interests.
- Correspondence** Correspondence and requests for materials should be addressed to R. M. (email: main@astro.utoronto.ca).
- Acknowledgements.** We thank A. Bilous for sharing and discussing her results which motivated this analysis. We thank the rest of our scintillometry group for discussions and support throughout. R.M., M.H.v.K., U.-L.P. and K.V. are funded through NSERC. I-S.Y was supported by a SOSCIP Consortium Postdoctoral Fellowship.

## Methods

**Calculating magnifications.** The data were taken in four 2.4 hr sessions on June 13–16, 2014, and were recorded as part of a European VLBI network program (GP 052). The data span 311.25–359.25 MHz, in three contiguous 16 MHz sub-bands, and we read, dedispersed (with a dispersion measure of 29.1162 pc/cm<sup>3</sup>), and reduced the data as described in ref <sup>11</sup>. As one extra step, we accounted for the wander in orbital period of PSR B1957+20 by adjusting the time of ascending node in the ephemeris, such that it minimized the scatter of the arrival times of giant pulses associated with the main pulse across all four days of observation.

We define the magnification of a pulse as the ratio of its flux to the mean flux in a quiescent region far from eclipse. Specifically, we construct an intensity profile of each pulse using 128 phase gates, subtract the mean off-pulse flux in each 16 MHz sub-band separately, measure the flux in an 8-gate ( $\sim 100 \mu\text{s}$ ) window around the peak location (which we find from folded profiles, averaged in 2 s bins to obtain sufficient signal-to-noise), and divide by the average flux in the same pulse window measured in a 9-minute section far from eclipse.

To construct the spectra of lensing events, we start by binning power spectra in 3 MHz bins. We correct these approximately for the bandpass and the effects of interstellar scintillation (which still has a small amount of power on 3 MHz scales) by dividing them by the average spectra in the 15 seconds before and after (excluding the lensing event itself). This time span is chosen to be safely less than the timescale of  $\sim 84$  s on which the interstellar scintillation pattern varies <sup>11</sup>, ensuring the dynamic spectrum is stable on these scales. With 30 s of data, it is also very well measured: each 3 MHz channel has  $S/N \simeq 150$ . **Evidence that strong plasma lensing must occur.** To obtain the properties of the lensed images, and in particular to determine whether we are in the “strong” or “weak” lensing regime – i.e., whether or not multiple images are formed – we use the basic principles of wave optics, considering path integrals of the electric field over a thin lens <sup>1</sup>. In our case, the phase of an electromagnetic wave going through different paths has contributions from both geometric and dispersive time delays,

$$\phi(x, y) = \phi_{\text{GM}}(x, y) + \phi_{\text{DM}}(x, y), \quad (2)$$

where  $x$  and  $y$  are in the lens plane. For a geometrically thin lens, i.e., with thickness along the line of sight much smaller than the separation  $a$ , the geometric contribution to the phase can be written as,

$$\phi_{\text{GM}} = \frac{1}{2} \left( \frac{x^2 + y^2}{a^2} \right) \left( \frac{a}{\lambda} \right) = \frac{x^2 + y^2}{2R_{\text{Fr}}^2}, \quad (3)$$

where  $R_{\text{Fr}}$  is the Fresnel scale,

$$R_{\text{Fr}} \equiv \sqrt{\lambda a} \simeq 40 \text{ km}, \quad (4)$$

with  $\lambda$  the wavelength of the radiation. For the numerical value, we used  $\lambda = c/\nu = 90 \text{ cm}$  (where  $\nu$  is the observing frequency) and assumed that the lensing material was associated with the companion and thus at the orbital separation of  $a \simeq 6.4 \text{ lt-sec}$ .

(Note that by using wavelengths and frequencies of full cycles, our phases are in cycles too, not radians.)

The dispersive contribution arises from the signal propagating through the lens’s extra dispersion measure (electron column density)  $\Delta DM = \int n_e dz$  (with  $n_e$  the electron number density),

$$\phi_{\text{DM}}(x, y) = -\frac{k_{\text{DM}}}{\nu} \Delta DM(x, y), \quad (5)$$

where  $k_{\text{DM}} = e^2/2\pi m_e c = 4148.808 \text{ s pc}^{-1} \text{ cm}^3 \text{ MHz}^2$  (ref. <sup>2</sup>). The minus sign arises because in a plasma the phase velocity is greater than the speed of light.

Integrating over different paths, one effectively select regions where the electric fields are coherent; these lead to the final images. For instance, if the extra electrons are distributed uniformly (in the  $x$ - $y$  plane after the  $z$  integral), then  $\phi_{\text{DM}}$  is approximately constant and the total phase has a stationary point around  $x = y = 0$ , i.e., around the line of sight. Furthermore, all paths which are less than the Fresnel scale away from this central path have similar phase, and thus one recovers the general result that the area of the lens that contributes scales with  $R_{\text{Fr}}^2$ .

For the lensing to be strong, a minimum requirement is that changes in the geometric and dispersive phase are of similar magnitude. Since dispersion also leads to overall time delays, differences in pulse arrival time give a handle on inhomogeneities in the lensing material. We measure pulse arrival times using the usual procedure of fitting pulse profiles to a high signal-to-noise template (from a quiescent period). We fit profiles in the three bands separately, and convert the weighted average to  $\Delta DM$  using standard equations. We find that the inferred  $\Delta DM$  shows both the expected large-scale variations<sup>7</sup> and significant variability down to the shortest time scales, of 2 s, at which we can measure it reliably (see Extended Data, Fig.3). During the periods in which the strongly magnified events occur, we find intrinsic variability corresponding to variations in delay of  $\Delta t_{\text{DM}} \simeq 1 \mu\text{s}$ , which suggests the inhomogeneities correspond to differences in the dispersion phase of  $\Delta \phi_{\text{DM}} = \nu \Delta t_{\text{DM}} \sim 300$  cycles at 2 s timescales.

To compare this to the geometric phase, we need to translate the timescale of 2 s to a length scale. Assuming the relative motion between the pulsar and the lensing material is dominated by the orbital motion, of 360 km/s, the spatial scale is 720 km. Using Eq. (3), this corresponds to  $\Delta \phi_{\text{GM}}(720 \text{ km}) \sim 200$  cycles.

The fact that  $\Delta \phi_{\text{DM}}$  is comparable and slightly larger than  $\Delta \phi_{\text{GM}}$  at the 720 km distance scale guarantees that somewhere around this scale, slopes in  $\phi_{\text{DM}}$  and  $\phi_{\text{GM}}$  will sometimes cancel. It also implies that multiple stationary points with  $\nabla \phi = 0$  are likely. Since the phases result from a continuous function of  $x$ ,  $y$  and  $\nu$ , the stationary points must emerge or annihilate in pairs, leading to so-called caustics, where one has not just  $\nabla \phi = 0$  but also  $\det(\partial_i \partial_j \phi) = 0$ <sup>3</sup>.

Given the above, strong lensing is a natural cause of the strongly magnified events we observe.

**A perfect lens model.** To calculate properties of the lensed images, we would need to perform the path integral. This is not possible since it requires the value of  $\phi_{\text{DM}}$  of the full two-dimensional lens plane at a resolution better than the Fresnel scale, while our time-delay measurements are limited to the one-

dimensional trajectory of the pulsar, and to an order of magnitude larger scales.

Hence, for our analysis we use a simplified model, amenable to wave-optics analysis, in which each strong lensing event is associated with an elliptical perfect lens, i.e., there is a single focal point to which all paths within the lens contribute perfectly coherently, and all paths outside the lens do not contribute at all. As shown in Extended Data Figure 2, our model is parametrized by the location of the focal point relative to the centre of the lens,  $(X, Y)$ , the semi-major and semi-minor axes of the lens,  $(\Delta x_{\text{lens}}, \Delta y_{\text{lens}})$ , and the orientation relative to the projected pulsar trajectory.

In the special case of a centred circular lens with radius  $R$ , i.e.,  $\Delta x_{\text{lens}} = \Delta y_{\text{lens}} = R$  and  $X = Y = 0$ , the setup would produce an Airy disk. By comparing this to the actual path-integral of an unlensed image (i.e., with  $\phi_{\text{DM}} = 0$ ), we can identify the unlensed case with a circular lens with radius  $R_1 \equiv R_{\text{Fr}}/\sqrt{\pi}$ .

Integrating the electric field over an elliptical lens, the magnification (defined as the increase in intensity  $\mu = I/\langle I \rangle$ , where  $I = E^2$ ), will be proportional to the area squared,

$$\mu = \left( \frac{\Delta x_{\text{lens}}}{R_1} \right)^2 \left( \frac{\Delta y_{\text{lens}}}{R_1} \right)^2. \quad (6)$$

Before continuing, we note that at first glance it might appear puzzling for the magnification to be proportional to image area squared, since that seems to violate energy (flux) conservation. However, the image is also more highly beamed; what we calculated is the magnification in the center of the beam. Viewed from an angle, a linear phase term is induced across the originally coherent region. Thus, when the region is larger, it is easier to become incoherent. The solid angle scales as  $\Delta\Omega \propto \Delta x_{\text{lens}}^{-1} \Delta y_{\text{lens}}^{-1}$ , and thus total energy (flux) is indeed proportional to the area of the lens.

**Differential magnification and chromaticity.** We now proceed to derive the physical resolution of the lens. The above magnification is reached only when the source is exactly at the focal point. When the emission region is some distance away from the focal point, paths from it to different parts of elliptical region will have extra phase differences. For instance, when a source is separated from the focal point in the  $x$  direction by  $x_{\text{source}} \equiv (X - x_s)$  (where  $x_s$  is measured relative to the centre of the lens), there is a phase difference across the lens of

$$\Delta\phi = \frac{\Delta x_{\text{lens}} x_{\text{source}}}{R_1^2}. \quad (7)$$

When this phase difference reaches order one, the image from the new source location will no longer be magnified. Defining the resolution as the offset for which total cancellation happens, we find from an explicit integral over the elliptical lens,<sup>1</sup>

$$x_{\text{res}} \simeq \frac{1.9R_1^2}{\Delta x_{\text{lens}}}, \quad (8)$$

$$y_{\text{res}} \simeq \frac{1.9R_1^2}{\Delta y_{\text{lens}}}. \quad (9)$$

<sup>1</sup>With a simple rescaling, the elliptical integral can be written as the circular one leading to an Airy disk.

Hence, total cancellation occurs on an elliptical beam with semi-minor and semi-major axes  $x_{\text{res}}$  and  $y_{\text{res}}$  that scale inversely to the semi-major and semi-minor axes of the lens.

We can write the above in terms of the magnification for a specific lens model. We will consider two extremes, the first a very anisotropic lens, effectively one-dimensional, for which  $\Delta y_{\text{lens}} = R_1$ . For this case,

$$x_{\text{res}} \simeq \frac{1.9R_1}{\mu^{1/2}}. \quad (10)$$

In the opposite direction, we consider a circular lens, with  $\Delta x_{\text{lens}} = \Delta y_{\text{lens}}$ . For this case,

$$x_{\text{res}} = y_{\text{res}} \simeq \frac{1.9R_1}{\mu^{1/4}}. \quad (11)$$

Here, dividing by the distance  $a$  and writing in terms of diameter  $D = 2\Delta x_{\text{lens}}$ , one recovers the usual relation for the angular resolution of a circular lens,  $1.22\lambda/D$ .

A similar result can be derived in frequency space. Given the different frequency dependencies of the geometric and dispersive phases, a lens cannot be fully in focus across all frequencies, but will have some characteristic frequency width. To show this, we first assume that the focal point is co-located with the centre of the elliptical lens, i.e.,  $(X, Y) = (0, 0)$ , and that perfect coherence occurs at some frequency  $\nu_c$ , i.e., that at  $\nu_c$  one has,

$$\phi_{\text{GM}}(x, y, \nu_c) = -\phi_{\text{DM}}(x, y, \nu_c) = \frac{\nu_c(x^2 + y^2)}{2ac}. \quad (12)$$

The total phase at a nearby frequency is then given by

$$\phi(x, \nu_c + \Delta\nu) = \left( \frac{\nu_c + \Delta\nu}{\nu_c} - \frac{\nu_c}{\nu_c + \Delta\nu} \right) \frac{\nu_c(x^2 + y^2)}{2ac}, \quad (13)$$

the dominant term of which is linear in  $\Delta\nu$ . If this term is of order one within the elliptical region, the image will no longer be magnified. Perfect cancellation does not happen in this case, but one can define characteristic width. Using half-width at half-maximum, one finds,

$$\left( \frac{\Delta\nu}{\nu_c} \right)_{\text{HWHM}} = \frac{2.9R_1^2}{\sqrt{3\Delta x_{\text{lens}}^4 - 2\Delta x_{\text{lens}}^2 \Delta y_{\text{lens}}^2 + 3\Delta y_{\text{lens}}^4}}. \quad (14)$$

In terms of the magnification, we find for the special case of an effectively one-dimensional lens,

$$\left( \frac{\Delta\nu}{\nu_c} \right)_{\text{HWHM}} \simeq \frac{1.7}{\mu}, \quad (15)$$

while for a circular lens,

$$\left( \frac{\Delta\nu}{\nu_c} \right)_{\text{HWHM}} \simeq \frac{1.5}{\mu^{1/2}}. \quad (16)$$

When the focal point is not in the center of the elliptical region, there will be linear terms proportional to  $X\Delta\nu$  and  $Y\Delta\nu$  that also contribute to the phase. They make the dependence on  $\Delta\nu$  even steeper, which means that Eq. 14 is an upper bound on the frequency width of magnified images.

It is possible for the frequency and position shifts to cancel each other, so that after moving the source by some distance,

it is still strongly magnified at a nearby frequency. That leads to a slope of strongest magnification in time-frequency space. Following a derivation similar to that outlined above for the behavior with frequency and position separately, we find that the slope is related only to the offset of the source from the focal point. For instance, for the case that the source is traveling along the semi-major axis of the lens, i.e., along a trajectory  $(x_s, y_s) = (x_s(t), 0)$ , we find

$$\frac{d\nu}{dx_s} = \frac{\nu_c}{2x_s}. \quad (17)$$

Finally, it is possible that the pulsar is close to the focus of more than one lens at the same time. As the pulsar moves, these multiple focal points lead to multiple images which change intensity and interfere with each other. This can lead to a wide variety of spectral behavior, and might well be responsible for the multi-peaked structures seen in some panels of Figure 2.

**A lower bound on the relative velocity.** Within the perfect lens approximation, one can derive a lower bound on the relative, transverse velocity between the lens and the pulsar using the durations and frequency widths of the lensing events.

The duration of strongly magnified events is predicted to be,

$$\Delta t_{\text{HWHM}} \simeq \frac{0.7R_1^2}{\sqrt{\Delta x_{\text{lens}}^2 v_x^2 + \Delta y_{\text{lens}}^2 v_y^2}} > \frac{0.7R_1^2}{v\Delta x_{\text{lens}}}, \quad (18)$$

where the inequality corresponds to making the most conservative estimate, that the lens is effectively one-dimensional, extended in the  $x$  direction, and that the full velocity  $v$  is directed along it.

In the frequency space, the same event will have its width bounded from above by Eq. (14),

$$\left(\frac{\Delta\nu}{\nu}\right)_{\text{HWHM}} < \frac{1.8R_1^2}{\Delta x_{\text{lens}}^2}. \quad (19)$$

Combining the two limits to eliminate  $\Delta x_{\text{lens}}/R_1$ , we find,

$$v > 0.5 \frac{R_1}{\Delta t_{\text{HWHM}}} \left(\frac{\Delta\nu}{\nu}\right)_{\text{HWHM}}^{1/2}. \quad (20)$$

**Lensing consistency checks.** Our analysis in terms of lensing was motivated by the fact that the bright pulses before and after eclipse do not look like giant pulses, that they occur at specific orbital phases where DM fluctuations are large, and that, in the majority of events, the entire profile increases in flux (although not always by the same factor across the profile), with the enhancements lasting for several pulses.

Consistent with the expectations of plasma lensing, in which lenses focus light but arrive with associated “shadows” where light is scattered away from our direct line of sight, we find that in regions with many strongly lensed pulses, the average flux received is unchanged (see Extended Data Figure 4). Also consistent with plasma lensing is that the strongly magnified pulses are highly chromatic, often peaking at high or low frequencies, and sometimes showing slopes in frequency time space or interference patterns characteristic of caustics.

Finally, as a concrete example, the peak magnifications of  $\mu \sim 70$  are comparable to the magnifications expected for

plasma lensing. The measured dispersive time delay changes provide direct evidence that the geometric and dispersive phases  $\phi_{\text{GM}}$  and  $\phi_{\text{DM}}$  can cancel over distances of  $\sim 720$  km. The cancellation will likely happen mostly in one spatial direction; setting  $\Delta x_{\text{lens}} = 720$  km and  $\Delta y_{\text{lens}} = R_1$ , our perfect lens model predicts a magnification of order a hundred, comparable to the observed value.

**Data Availability.** The data underlying the figures is available in text files at

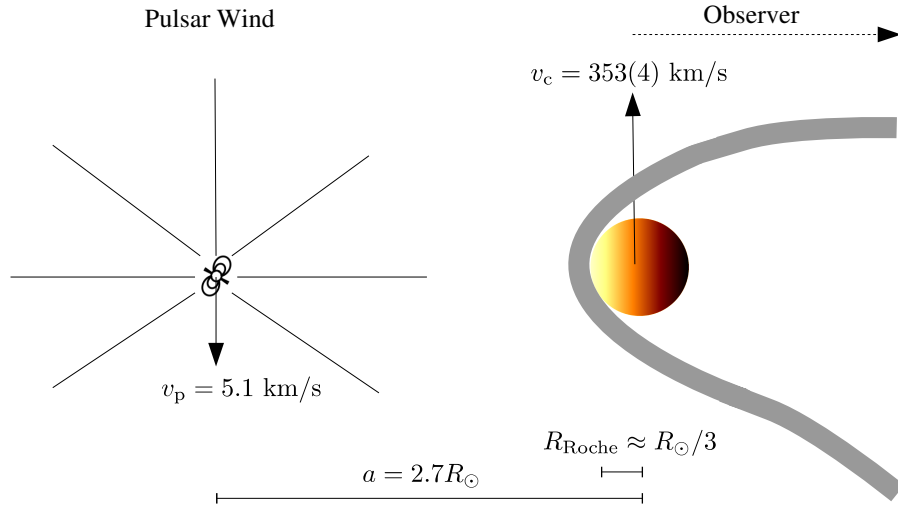
<https://github.com/ramain/B1957LensingData>

**Code Availability.** The raw data were read using the baseband package:

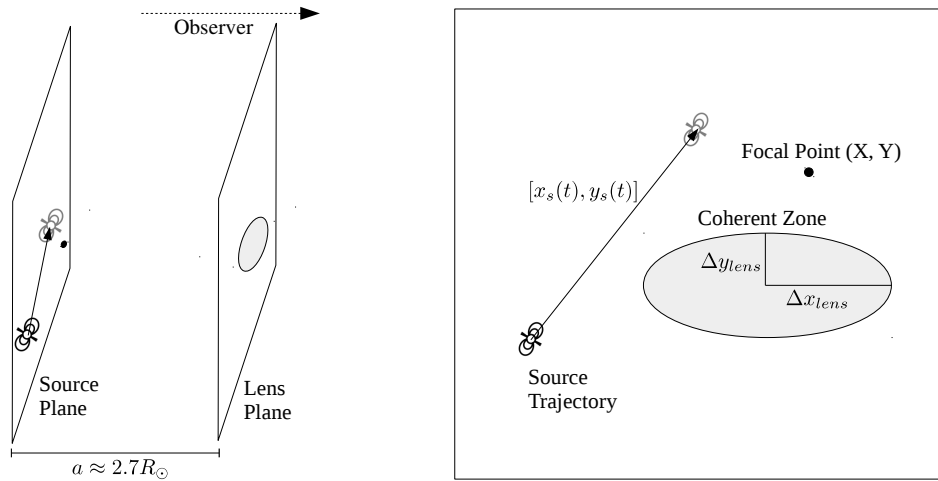
<https://github.com/mhvk/baseband>

1. Born, M. & Wolf, E. *Principles of optics : electromagnetic theory of propagation, interference and diffraction of light* (1999).
2. Manchester, R. N. & Taylor, J. H. Parameters of 61 Pulsars. *Astrophysics Letters* **10**, 67 (1972).
3. Nye, J. F. *Natural focusing and fine structure of light: caustics and wave dislocations* (1999).
4. van Paradijs, J. *et al.* Optical observations of the eclipsing binary radio pulsar PSR1957 + 20. *Nature* **334**, 684–686 (1988).
5. Reynolds, M. T. *et al.* The light curve of the companion to PSR B1957+20. *Monthly Notices of Royal Astronomical Society* **379**, 1117–1122 (2007). 0705.2514.

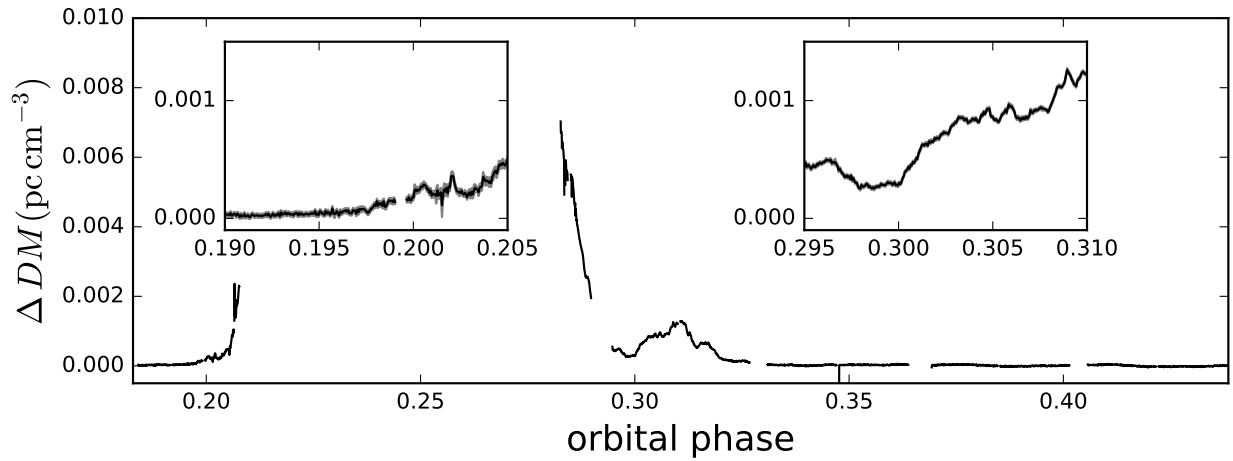
## Extended Data



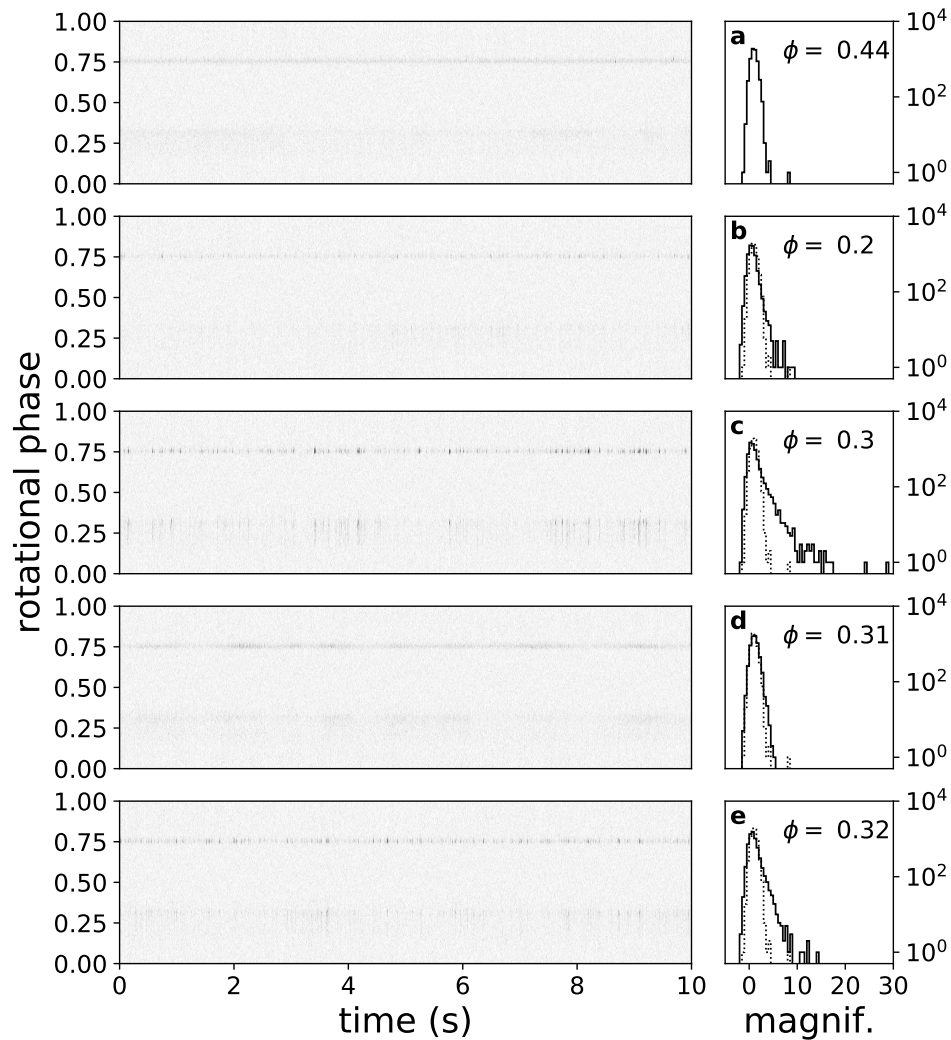
Extended Data Figure 1: **Shock geometry.** The brown dwarf companion is irradiated by the pulsar wind<sup>4</sup>, and inflated, nearly filling its Roche lobe<sup>5</sup>. Outflowing material is shocked by the pulsar wind, leaving a cometary-like tail of material. This tail is asymmetric because of the companion’s orbital motion, which leads to eclipse egress lasting substantially longer than ingress. The companion and separations are drawn roughly to scale, while the pulsar is not – the light cylinder radius of 76 km would be indistinguishable on this figure. The inclination of the system is conservatively constrained to  $50 < i < 85$  deg (ref. <sup>13</sup>).



Extended Data Figure 2: **Geometry of a lensing region.** An almost edge-on (left) and a face-on (right) view of the lensing geometry. We assume that the source is at a separation equal to the semi-major axis  $a$  of the binary system and moves on a trajectory parallel to the lens plane. A source at the focal point  $(X, Y)$  will illuminate the entire elliptical lens coherently, leading to strong magnification. In general, the focal point may not be at the center of the ellipse (although it is likely within it), and the source trajectory  $[x_s(t), y_s(t)]$  may not intersect the focal point or the elliptical region.



Extended Data Figure 3: **Dispersion measure near the radio eclipse.** Shown is the excess dispersion measure relative to the interstellar dispersion, with insets focusing on regions of strong lensing. The excess dispersion is estimated from delays in pulse arrival times (see Methods); at our observing frequency of 330 MHz,  $\Delta DM = 0.001 \text{ pc cm}^{-3}$  corresponds to a delay of  $38 \mu\text{s}$ . The scatter around the curves is intrinsic. During periods of strong lensing, it is at a level of  $2.6 \times 10^{-5} \text{ pc cm}^{-3}$ , corresponding to variations in delay time of  $1 \mu\text{s}$ .



Extended Data Figure 4: **Pulse profiles and magnification distributions.** Each row shows pulse profiles for 10 s segments (left, in 128 phase bins), and the corresponding magnification distributions. The segments are taken from: **a**, a quiescent region, showing a log-normal magnification distribution (repeated using a dotted line in **b–e** for comparison); **b**, eclipse ingress, showing some lensing events, reflected in the tail to high magnification; although hard to see, the average flux is reduced to  $\sim 70\%$  by absorption in eclipsing material); **c**, the first post-eclipse lensing period, showing extreme magnifications but little change in average flux; **d**, in between the two post-eclipse strong lensing periods, showing only weak lensing on relatively long,  $\sim 100$  ms timescales; **e**, the second post-eclipse period of strong lensing.